

APPLICATION OF THE FINITE-VOLUME METHOD TO FLUID-STRUCTURE INTERACTION ANALYSIS

Tim Craft, Hector Iacovides, Matthew Yates

Department of Mechanical, Aerospace and Civil Engineering,
University of Manchester, Manchester, M60 1QD, UK
m.yates@postgrad.manchester.ac.uk

ABSTRACT

This paper describes the numerical simulation of steady flow through severely stenosed tubes and the development of a fully coupled fluid-solid solver, capable of predicting the effects of fluid pressure and wall shear stress on the elastic tube wall. This particular type of interaction occurs commonly in physiological flows. Whilst geometrically simple, even with a rigid wall this type of flow exhibits many complex phenomena such as re-circulation and transition to turbulence, both of which make numerical simulation difficult.

Initially, flow simulations are reported for a rigid walled tube over a range of physiologically relevant flow rates. Laminar simulations were only successful for Reynolds numbers of less than 300; deviation from the experimental data occurred at the experimentally observed point of transition. Computations using a low-Reynolds-number turbulence model proved successful for Reynolds numbers greater than 1500, with results being in good agreement with experimental data.

Following these rigid-wall CFD simulations, a finite-volume based method for solving solid body stress analysis problems has been developed, and the results of a validation exercise show good agreement with analytical solutions. This solid body solver has then been coupled to the CFD code to allow fully coupled fluid-structure interaction (FSI) analyses of flow through a compliant walled stenosis to be performed. Initial results from such coupled cases show a reasonably accurate response of the wall deformation to the flow rate.

INTRODUCTION

Arterial stenoses are a commonly occurring problem in humans and a proper understanding of their effects is important to develop future treatments. Whilst their cause is not completely understood, the most commonly given reason is the accumulation of atherosclerotic plaque on the inside of artery walls (Young, 1979). The reduction in cross sectional area caused by the stenosis can have significant impact on the local hydrodynamics, which in turn can cause additional stenosis growth or other physiological problems.

The purpose of the work described in this paper is to numerically simulate the coupled system of fluid flow and compliant wall displacement through a severely stenosed tube. This has firstly involved studying the fluid dynamics in a rigid walled tube - particularly finding suitable turbulence representation at transitional Reynolds numbers. In parallel, a finite-volume based solid body stress analysis code has been developed and validated. Finally, the fluid flow and stress analysis codes have been combined and used to simulate the fully coupled system.

Both laminar and turbulent simulations have been performed in an attempt to cover a range of physiologically

realistic flow rates. Only steady flow has been considered thus far. The fluid has been modelled as Newtonian with constant physical properties, which is a valid assumption in the larger arteries.

Young and Tsai (1973) performed experiments of steady flow through rigid walled tubes with both axisymmetric and non-symmetric stenosis of varying lengths and area constrictions. Reynolds numbers ranged between 100 and 5000. Measurements were made of the pressure drop across the stenosis and of the re-circulation region size. The main finding of this work is that for tubes with severe stenosis, area constriction of 89%, the transition to turbulence occurs at much lower Reynolds numbers than would be observed in straight tubes.

Ahmed and Giddens (1983) also conducted experiments of steady flow through rigid stenosed tubes. Detailed mean and fluctuating velocity profiles were measured by laser Doppler anemometry, whilst qualitative information was found through hydrogen bubble visualisation. The Reynolds number was in the range 500 to 2000, whilst stenosis severities of 25, 50 and 75% were used. The flow visualisation for the most severe stenosis indicated the presence of periodic oscillations in the shear layer between the core flow jet and the re-circulation region at $Re = 500$; as the flow rate increased these oscillations were replaced with random fluctuations. Radial velocity profiles show that the re-attachment point moves downstream with increasing Reynolds number, until transition to turbulence occurs, after which it moves back upstream. Measurements show that the axial velocity increases by a factor of 4 distal to the throat of the stenosis due to the area reduction, before decaying back to the proximal level after 2 diameters. The peak centreline disturbance intensity occurred 3.5 diameters from the throat. The main finding of the work is that for severe stenosis, discrete oscillations or even turbulence can occur at relatively low Reynolds numbers; something which must be taken into account when numerically simulating such a flow.

Ghalichi et al. (1998) numerically simulated steady flow through a number of rigid stenosis models using a low-Reynolds-number form of the $k-\omega$ model of Wilcox. Stenosis severity varied between 50 and 86% whilst the Reynolds number was in the physiological range. The numerical results were compared to the experimental data of Ahmed and Giddens. At lower flow rates, the size of the re-circulation region was found to increase linearly with Reynolds number, until a critical value was reached, at which point the re-circulation region reduced in size. For a stenosis of 89% severity, the critical Reynolds number was 260. Some of the results, namely streamwise variation of pressure and turbulence intensity were compared to numerical results obtained with the standard $k-\epsilon$ model. Whilst the $k-\omega$ model was shown to better predict the pressure recovery and increase in k downstream of the throat, this was most likely due to

the fact that the k - ϵ model employed did not include any additional low-Re terms.

Stergiopoulos et al. (1993) performed experiments of steady flow through a compliant walled stenosis. The area reduction at the throat of the stenosis was 90% and the length of the stenosis was 3.75 diameters. The compliant stenosis model was placed inside a water filled tank which reportedly applied a uniform external pressure of 3 mmHg. The pressure upstream of the stenosis was held constant at 74 mmHg whilst the downstream pressure was incrementally reduced. Flow rate and throat diameter measurements were made at each pressure difference. The results showed an almost linear decrease in throat diameter with pressure difference until a critical value was reached, at which point the elastic tube collapsed.

In this work, the initial focus of attention is on the rigid walled stenosis case experimentally investigated by Young and Tsai, the objective being to establish what turbulence modelling strategies are necessary for the reliable and efficient computation of flow through stenoses with rigid walls. A finite-volume based stress analysis code has then been developed and validated. Having verified the two codes individually, they have been combined to allow fully coupled fluid-structure analyses to be performed. The coupled solver has then been validated by computing the case experimentally investigated by Stergiopoulos et al.

CASE STUDIED

The first geometry modelled here matches model M2 used by Young and Tsai, and consisted of a straight inlet tube section of length 8.5 diameters. The stenosis was sinusoidal in shape and had a length of 4 diameters. The reduction in area at the throat of the stenosis was 89%. Downstream of the stenosis was a straight outlet section. For the turbulent flow calculations the length of the outlet section was 25 diameters, whilst for the laminar calculations the length was increased to 110 diameters to allow the flow to fully re-attach upstream of the exit. The grid used in the turbulent flow calculations consisted of 1780 nodes in the streamwise direction and 120 nodes in the radial direction; that used in the laminar calculations consisted of 2800 and 58 nodes in the streamwise and radial direction respectively. Such fine resolution in the radial direction is necessary when using a low-Re turbulence model as the governing equations are integrated through the viscous-sublayer where sharp gradients of flow variables occur. A schematic of the geometry is given in Figure 1.

MATHEMATICAL MODEL FOR FLUID MOTION

Flow simulations have been performed using the in-house CFD code STREAM (Lien and Leschziner, 1994). This is a finite-volume based code which solves the steady incompressible Navier-Stokes equations using the SIMPLE pressure-velocity coupling and UMIST second-order convective discretization scheme. A collocated storage arrangement is used with Rhie and Chow (1983) interpolation to ensure the correct pressure-velocity linkage and avoid pres-

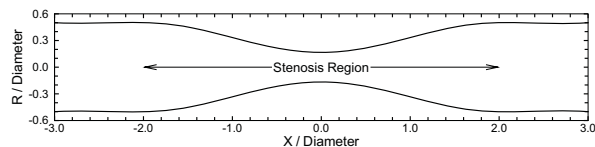


Figure 1: Schematic of stenosis geometry.

Table 1: Coefficients used in the Launder-Sharma model.

$c_{\epsilon 1}$	$c_{\epsilon 2}$	c_{μ}	σ_k	σ_{ϵ}
1.44	1.92	0.09	1.0	1.3

sure chequer-boarding. A boundary fitted non-orthogonal grid with Cartesian velocity decomposition is used to increase geometric versatility. The pipe flow was computed by assuming the flow to be axisymmetric. At low Reynolds numbers the laminar flow equations were solved, whilst at higher Reynolds numbers the RANS equations were solved. In the latter case the Reynolds stresses were modelled with the Boussinesq linear stress-strain relation. The turbulent viscosity was obtained from the Launder-Sharma low-Re k - ϵ model (Launder and Sharma, 1974), which includes terms to account for viscous effects in the near wall region. The RANS form of the mass continuity equation, written in Cartesian tensor notation, is given by:

$$\frac{\partial U_i}{\partial x_i} = 0 \quad (1)$$

and the momentum equations are given by:

$$\frac{\partial}{\partial x_j} (U_i U_j) = -\frac{1}{\rho} \frac{\partial P}{\partial x_i} + \frac{\partial}{\partial x_j} \left(\nu \frac{\partial U_i}{\partial x_j} - \overline{u_i u_j} \right) \quad (2)$$

where uppercase letters represent mean flow variables and lowercase letters represent fluctuating variables. The turbulent stresses appearing in the above equation are related to the mean flow variables by:

$$\overline{u_i u_j} = \frac{2}{3} k \delta_{ij} - \nu_t \left(\frac{\partial U_i}{\partial x_j} + \frac{\partial U_j}{\partial x_i} \right) \quad (3)$$

The turbulent viscosity, ν_t , is obtained from:

$$\nu_t = f_{\mu} c_{\mu} \frac{k^2}{\epsilon} \quad (4)$$

The turbulent kinetic energy, k , and the isotropic dissipation rate, ϵ , are found by solving the following transport equations:

$$\frac{Dk}{Dt} = P_k - \bar{\epsilon} - 2\nu \left(\frac{\partial k^{1/2}}{\partial x_j} \right)^2 + \frac{\partial}{\partial x_j} \left[(\nu + \nu_t / \sigma_k) \frac{\partial k}{\partial x_j} \right] \quad (5)$$

$$\frac{D\bar{\epsilon}}{Dt} = c_{\epsilon 1} \frac{P_k \bar{\epsilon}}{k} - c_{\epsilon 2} f_2 \frac{\bar{\epsilon}^2}{k} + 2\nu \nu_t \left(\frac{\partial^2 U_i}{\partial x_j \partial x_k} \right)^2 + \frac{\partial}{\partial x_j} \left[(\nu + \nu_t / \sigma_{\epsilon}) \frac{\partial \bar{\epsilon}}{\partial x_j} \right] + S_{\epsilon} \quad (6)$$

The near wall damping functions are given by:

$$f_{\mu} = \exp \left[\frac{-3.4}{(1 + R_t/50)^2} \right] \quad (7)$$

$$f_2 = 1 - 0.3 \exp(-R_t^2) \quad (8)$$

where the turbulent Reynolds number is given by $R_t = k^2 / \epsilon \nu$. The constants used in the model are shown in Table 1. The S_{ϵ} term appearing on the right hand side of Equation 6 is the Yap lengthscale correction term. This has the effect of reducing the computed turbulent lengthscale in the re-circulation bubble, and is given by:

$$S_{\epsilon} = c_w (\epsilon^2 / k) \max \left[\left(\frac{l}{l_e} - 1 \right) \left(\frac{l}{l_e} \right)^2, 0 \right] \quad (9)$$

where $l \equiv k^{3/2} / \epsilon$ is the turbulent length scale and l_e the equilibrium length scale, $c_l y$, where $c_l = 2.55$ and y is the

near wall distance. The constant c_w has been empirically determined as 0.83 by Yap (1987).

FLUID FLOW RESULTS AND DISCUSSION

Laminar Results

It can be seen from the separation and re-attachment curve (Figure 2) that the point of flow separation was accurately predicted at low Reynolds numbers by the laminar solver. The point of separation moves slightly upstream towards the throat of the stenosis with increasing Reynolds number. The re-attachment length, which was identified by the point where the wall shear stress was equal to zero, is slightly under predicted when compared with the experimental data. However, Young and Tsai report that the location of the re-attachment point was more difficult to measure accurately than the separation point. The re-attachment point shows a much stronger dependence on the Reynolds number.

At Reynolds numbers greater than 200 the re-circulation bubble becomes very large, as shown in Figure 4. This means that the computational domain has to extend far downstream to allow the flow to once again become fully developed. This is important to ensure that the outlet boundary conditions are valid and do not introduce any significant error.

Figure 3 shows that the pressure drop across the stenosis is accurately predicted in the laminar regime. The non-dimensional pressure drop is greatest at lower Reynolds numbers where the viscous effects are dominant. Fully converged solutions were only achievable for Reynolds numbers of less than 700 by which stage the re-attachment length was around 45 diameters. However, it can be seen from Figure 3 that the pressure drop is most accurately predicted at Reynolds numbers less than 300; this coincides with the experimentally observed point of transition to turbulence. Even if the flow were to remain laminar beyond this point, the presence of the long re-circulation bubble would most likely mean that it would no longer be steady, which offers an explanation as to why the steady-state laminar computations fail to accurately predict the pressure drop at higher Reynolds numbers.

Turbulent Results

To produce accurate predictions at higher Reynolds numbers, the effects of turbulence must be accounted for. However, it was still found to be difficult to obtain a numerically stable solution at moderate Reynolds numbers due to the

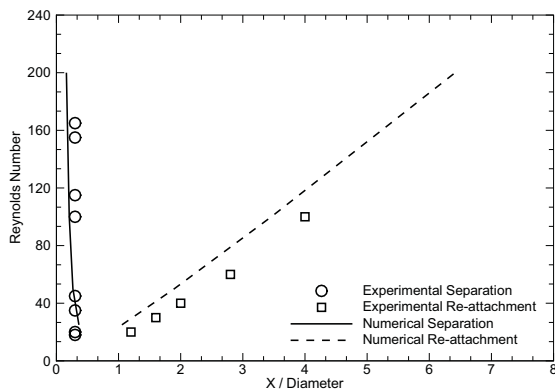


Figure 2: Separation and re-attachment curves for laminar flow.

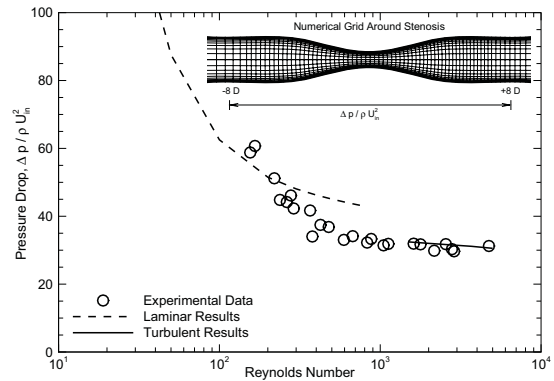


Figure 3: Pressure drop across stenosis.

transitional nature of the flow. What makes these flows especially difficult to converge using the RANS approach is that for low Reynolds numbers the flow is laminar upstream of the stenosis and only undergoes transition to turbulence after the separation point. Some of these difficulties were overcome by using the low-Reynolds-number Launder-Sharma model and by prescribing an initial flow field with non-zero turbulence over the entire flow domain. It can be seen from Figure 3 that the pressure drop is accurately predicted at Reynolds numbers greater than 1500. Converged solutions were not achievable for Reynolds numbers less than 1500.

The flow streamlines shown in Figure 5 indicate that the re-circulation bubble reduces in size with increasing Reynolds number. Both the separation and re-attachment point move upstream with increasing Re. The reduction in size of the re-circulation bubble is due to the increased mixing caused by the large turbulent fluctuations. By comparing the turbulent flow streamlines (Figure 5), with the laminar flow streamlines (Figure 4), the dramatic reduction in re-circulation bubble size due to the effects of turbulence can be seen.

Figure 5 also shows contours of the turbulent kinetic energy, k , with increasing Reynolds number. It can be seen that a region of high k develops downstream of the stenosis; this is due to the high shear rates in the separated shear layer. The region of high k moves upstream with increasing Reynolds number. The region of low k upstream of the throat indicates that the flow here is essentially laminar, before transition to turbulence occurs slightly downstream of the throat. Further downstream, beyond reattachment, turbulence levels decay back towards the laminar state.

MATHEMATICAL MODEL FOR SOLID DISPLACEMENT

In addition to the work described thus far, efforts have been made to develop a finite-volume based method for the solution of solid body stress analysis problems. This has been done to allow constricted pipe flow simulations to include compliant wall effects.

The method is based on the finite-volume discretization of the equations governing displacement in an elastic body. The equations governing steady-state stress equilibrium, written in Cartesian tensor notation, are given by:

$$\frac{\partial \sigma_{ij}}{\partial x_j} + f_i = 0 \tag{10}$$

where σ_{ij} represents a stress acting in the positive i direction on a face whose normal is in the positive j direction and f_i is the body force in the i direction. The stresses are related to the strains by the thermo-elastic constitutive equations:

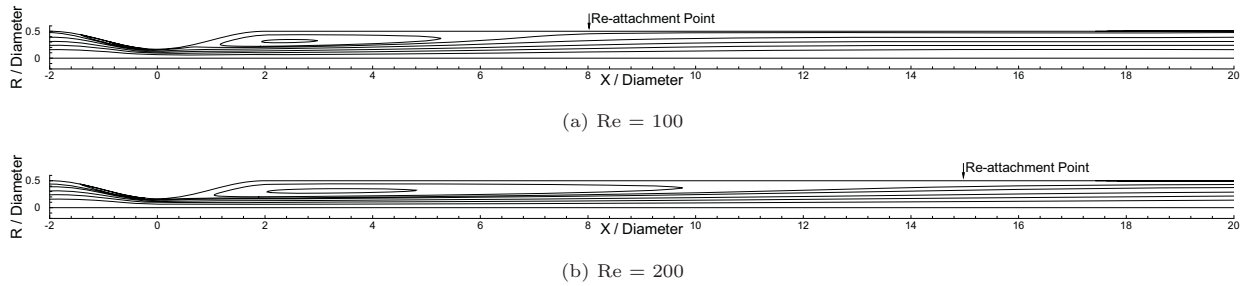


Figure 4: Laminar flow streamlines for increasing Reynolds number.

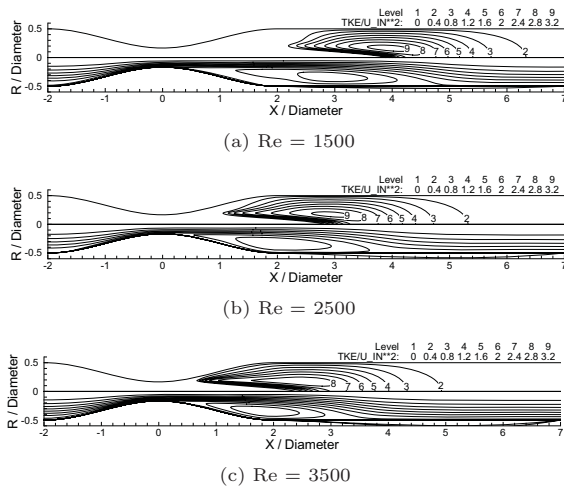


Figure 5: Flow streamlines (below line of symmetry) and contours of turbulent kinetic energy (normalized with respect to U_{in}^2) for increasing Reynolds number.

$$\sigma_{ij} = 2\mu\epsilon_{ij} + \lambda\delta_{ij}\epsilon_{kk} - (3\lambda + 2\mu)\delta_{ij}\alpha\Delta T \quad (11)$$

The use of these constitutive relations will also allow the effects of thermal stresses to be accounted for in future work. The strains are linked to the displacement gradients by the kinematic relation:

$$\epsilon_{ij} = \frac{1}{2} \left(\frac{\partial u_i}{\partial x_j} + \frac{\partial u_j}{\partial x_i} \right) \quad (12)$$

These three equations are combined to form Navier's displacement equations. These second order PDE's which govern the displacement vector, u_i , are then integrated over each computational cell. Face values of the displacement gradient are approximated by central differences; for example, the gradient of ϕ on the east face of a simple rectangular cell is given by:

$$\frac{\partial \phi}{\partial x} \Big|_e = \frac{\phi_E - \phi_P}{\Delta x} \quad (13)$$

Once all of the gradients have been replaced in this manner one is left with a system of linear equations for the displacements, together with appropriate traction, displacement or symmetry boundary conditions. The system is solved with the tri-diagonal matrix algorithm and the calculated displacements can be post-processed to give the stress field. The method is capable of solving both planar and axisymmetric problems. As with the fluid solver, the boundary fitted non-orthogonal coordinate system is used.

The method has been validated by simulating the stress field in a square plate with a circular hole in the centre subjected to uni-axial tension. The numerical solution was compared to the analytical solutions for an infinitely large

plate. Due to the symmetry of the problem, only one quarter of the plate needed to be considered. The analytical stresses were applied along the north and east boundaries of the domain to remove the effect of the plate's finite dimensions. Symmetry boundary conditions were applied along the west and south boundaries whilst a zero traction condition was applied along the circumference of the hole. The analytical solution for an infinitely large plate with a hole in the centre, subjected to a uniform uni-axial tensile force $f_x = 10$ kN in the x -direction, as given by Demirdžić and Muzafnerija (1994) is:

$$\sigma_{xx} = f_x \left[1 - \frac{a^2}{r^2} \left(\frac{3}{2} \cos 2\theta + \cos 4\theta \right) + \frac{3}{2} \frac{a^4}{r^4} \cos 4\theta \right] \quad (14)$$

$$\sigma_{yy} = f_x \left[-\frac{a^2}{r^2} \left(\frac{1}{2} \cos 2\theta - \cos 4\theta \right) - \frac{3}{2} \frac{a^4}{r^4} \cos 4\theta \right] \quad (15)$$

$$\tau_{xy} = f_x \left[-\frac{a^2}{r^2} \left(\frac{1}{2} \sin 2\theta + \sin 4\theta \right) + \frac{3}{2} \frac{a^4}{r^4} \sin 4\theta \right] \quad (16)$$

The comparison between the numerical and analytical solution for the normal stress in the x -direction is shown in Figure 6. The other stress components show a similar level of agreement. The largest discrepancy occurs at the north of the hole which could be due to the relatively skewed grid in this region.

In addition to solving stress analysis problems, the above method is also capable of producing high quality numerical grids for use in other simulations. In fact, the grid used in the flow simulations was produced by the solid solver. To achieve this the grid is considered to be a solid body with arbitrary material properties. An initial numerical mesh is defined which broadly describes the geometry of the desired final grid. Displacement boundary conditions are then applied on all boundaries to deform the grid to the desired geometry. The key feature of this method is the preservation of interior node distribution, such as near wall clustering; something which is difficult to do using elliptical grid generation. The method is particularly well suited to deforming

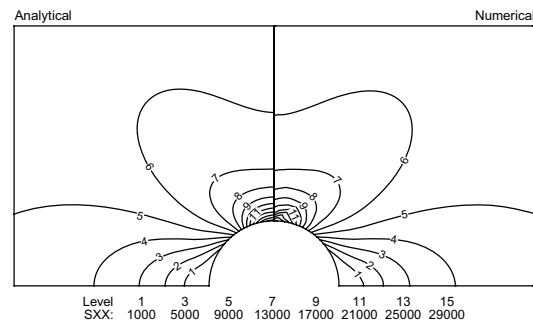


Figure 6: Results from the plate with a hole validation exercise. Calculated stress contours on the right hand side, analytical contours on the left. Contour levels chosen to replicate the plot given in Demirdžić and Muzafnerija (1994).

the numerical mesh during coupled FSI simulations; something which is vitally important to accurately predict the exchange of energy between the two regions.

COUPLED FSI RESULTS AND DISCUSSION

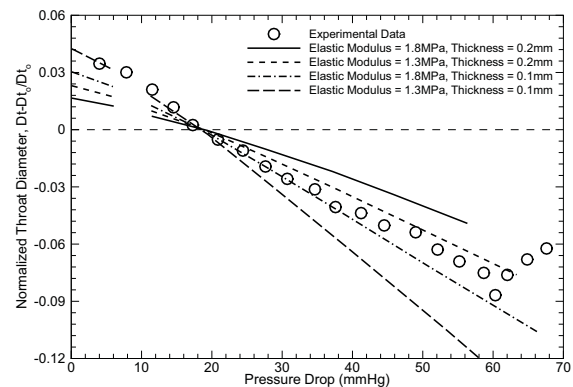
The newly developed finite-volume solid solver has been coupled to the CFD code described in earlier sections. The method has been implemented in a manner consistent with the STREAM code, to allow simple and efficient coupling. This avoids the need for inefficient software interfaces to transfer information between separate packages. Another feature of the new method is that a single numerical grid covers the entire domain, the fluid and solid solvers simply being applied over their respective sub-domains. Initially, the fluid solver calculates the flow over the fluid sub-domain; the resulting pressure and wall shear stress being applied as traction boundary conditions to the solid solver. Next, the solid solver calculates the displacements within the solid sub-domain. Finally, the calculated displacements along the interface are used to adapt the fluid mesh. The whole process is then repeated until overall convergence has been achieved.

The coupled solver has been validated by simulating flow through an elastic walled tube with an axisymmetric stenosis and the results have been compared with the experimental data of Stergiopoulos et al. (1993) and the numerical results of Shim and Kamm (2002).

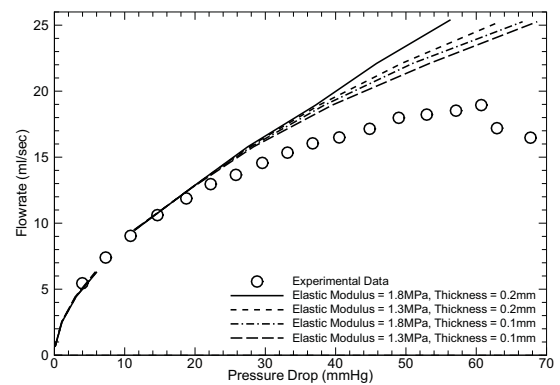
The fully coupled FSI simulation was set up to mimic the experiment described in the paper by Stergiopoulos et al. (1993). The physical geometry consists of a straight tube of diameter 8 mm and length 8.75 diameters, followed by a sinusoidal stenosis of length 3.75 diameters and area reduction of 90% and finally a straight outlet region of length 135 diameters. An elastic wall extends from 5 diameters upstream of the stenosis throat to 5 diameters downstream of the throat. The material is considered to be linear elastic with Poisson ratio, $\nu = 0.475$. The elastic wall is subject to zero displacement boundary conditions along its east and west faces. Traction boundary conditions are prescribed from the imposed external pressure on the north face and from the fluid flow solution pressure and wall shear on the south face. Both laminar and turbulent calculations were performed to cover the entire range of physiologically relevant Reynolds numbers.

Whilst Stergiopoulos et al. (1993) give the above information regarding the geometry of the stenosis and the physical properties of the working fluid, no mention is made of the vitally important material properties and wall thickness of the elastic tube or the exact location at which the reference pressure was measured. These three pieces of information govern the displacement of the elastic tube wall. To obtain good estimates of the required information, two tests were performed: firstly, a rigid walled CFD simulation was performed at the flow rate for which the experiment reported zero wall displacement. The reference pressure was then chosen so that the pressure difference between the inside and outside of the wall at the throat of the stenosis was zero. The result of this test was that the external pressure had to be increased from the reported 3 mmHg to 42.1 mmHg. This pressure can easily be verified by application of Bernoulli's equation between the tube inlet and the stenosis throat. Analytical calculations show that pressure losses are negligibly small compared to Bernoulli losses over these tube lengths. Secondly, sensitivity tests were conducted by varying the tube wall thickness and elastic modulus, the objective being to accurately predict the throat diameter variation with in-

creasing flow rate. The elastic modulus was varied between 1.3 – 1.8 MPa, which is slightly lower than the range measured experimentally by Schneider et al. (2008). The wall thickness was varied between 0.1 – 0.2 mm.



(a) Normalized throat diameter comparison.



(b) Volumetric flow rate comparison.

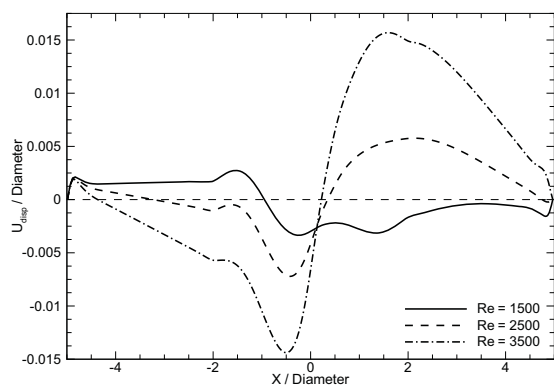
Figure 7: Comparison of throat diameter and flow rate as a function of pressure drop across stenosis.

Figure 7 shows a comparison between the numerical and experimental results. Converged solutions were unobtainable between Reynolds numbers of 1000 and 1500, due to the difficulties in capturing transition described in earlier sections. Simulations were also not performed beyond the point at which the experiments reported tube collapse as the current axisymmetric model is not able to capture such an asymmetric phenomena.

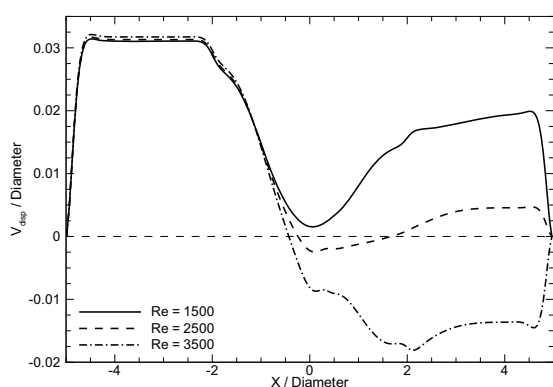
The measured throat diameter decreases almost linearly with flow rate until a critical flow rate is reached at which point the tube collapses. As a result of the first test described above, the key point of zero displacement is accurately predicted. The effect of reducing the elastic modulus and the thickness of the tube wall is an increased rate at which the throat diameter varies with flow rate. The experimental data is most closely matched by setting the elastic modulus to 1.3 MPa and the wall thickness to 0.2 mm. Whilst the results shown in Shim and Kamm (2002) show a similar level of agreement, the absence of a turbulence model in their simulations limited them to low flow rates.

The pressure drop across the stenosis shows good agreement with the experimental data at low flow rates. However, at flow rates greater than 15 ml/sec, the numerical results under-predict the pressure drop. It is thought that this could be due to the fact that at higher flow rates the elastic tube may have deformed into an asymmetric cross-section. The results from the rigid walled CFD simulations presented ear-

lier suggest that the flow solver is able to accurately predict the pressure drop across an axisymmetric stenosis at high flow rates. The variation of the elastic modulus and wall thickness has only a small effect on the pressure drop. This could be due to the fact that the pressure drop is measured over the full length of the elastic region, after pressure recovery downstream of the throat, and thus does not depend strongly on the exact deformation at the throat.



(a) Axial displacement.



(b) Radial displacement.

Figure 8: Normalized wall displacement profiles for increasing Reynolds number with $E = 1.3 \text{ MPa}$ and $t = 0.2 \text{ mm}$.

The displacement profiles of the tube wall (normalized with respect to inlet tube diameter) in Figure 8 show how the throat diameter reduces with increasing flow rate. At low flow rates the radial displacement at the throat of the stenosis is positive, because the external pressure is lower than the internal pressure at the throat. As the flow rate is increased, the pressure drop at the throat reduces and becomes lower than the external pressure. This causes the radial displacement of the tube at the throat to become negative. As the flow rate is further increased, the pressure in the entire downstream region becomes lower than the external pressure, resulting in negative radial displacement from the throat to the end of the elastic region. At even higher flow rates, the location of the maximum (negative) radial displacement moves downstream from the throat.

CONCLUDING REMARKS

This paper has described the numerical simulation of flow through a severely stenosed tubes. Flow in the rigid wall case was generally well captured in both the laminar and turbulent regimes. Converged solutions were, however, difficult to obtain at intermediate Reynolds numbers of $700 - 1500$, due to the nature of transition occurring in the separated

shear layer, well downstream of the throat. A finite-volume based solid solver has been developed and validated against existing analytical results. The solid solver is also capable of producing and adapting numerical grids. The fluid and solid codes have then been coupled and applied to the compliant walled stenosis case. Results have generally shown good agreement with existing measurements in terms of the pressure drop and wall deflection of the throat over a range of flow rates.

Future attention will be focused towards simulating flow through an abdominal aortic aneurysm (AAA). Both steady and pulsatile flow will be considered for both rigid and compliant walled AAA models. This will provide a better understanding of another important category of physiological flow.

ACKNOWLEDGEMENT

Matthew Yates acknowledges with thanks the financial support of the Douglas Prestwich Trust during this work.

REFERENCES

- S. A. Ahmed and D. P. Giddens. Velocity measurements in steady flow through axisymmetric stenoses at moderate Reynolds numbers. *Journal of Biomechanics*, 16(7):505–516, 1983.
- I. Demirdžić and S. Muzaferija. Finite volume method for stress analysis in complex domains. *Int. J. for Numerical Methods in Engineering*, 37:3751–3766, 1994.
- F. Ghalichi, X. Deng, A. De Champlain, Y. Douville, M. King, and R. Guidoin. Low Reynolds number turbulence modelling of blood flow in arterial stenoses. *Biorheology*, 35: 281–294, 1998.
- B. E. Launder and B. I. Sharma. Application of the energy-dissipation model of turbulence to the calculation of flow near a spinning disk. *Letters in Heat and Mass Transfer*, 1: 131–138, 1974.
- F. S. Lien and M. A. Leschziner. A general non-orthogonal collocated finite volume algorithm for turbulent flow at all speeds incorporating second-moment turbulence-transport closure, Part 1: Computational implementation. *Comput. Methods Appl. Mech. Engrg.*, 114:123–148, 1994.
- C. M. Rhie and W. L. Chow. Numerical study of the turbulent flow past an airfoil with trailing edge separation. *AIAA Journal*, 21:1525–1532, 1983.
- F. Schneider, T. Fellner, J. Wilde, and U. Wallrabe. Mechanical properties of silicones for MEMS. *Journal of Micromechanics and Microengineering*, 18:065008, 2008.
- E. B. Shim and R. D. Kamm. Numerical simulation of steady flow in a compliant tube or channel with tapered wall thickness. *Journal of Fluids and Structures*, 16(8):1009–1027, 2002.
- N. Stergiopoulos, J. E. Moore, A. Strässle, D. N. Ku, and J. J. Meister. Steady flow tests and demonstration of collapse on models of compliant axisymmetric stenoses. *Advances in Bioengineering*, BED-26:455–458, 1993.
- C. R. Yap. *Turbulent Heat and Momentum Transfer in Recirculating and Impinging Flows*. PhD thesis, Faculty of Technology, University of Manchester, 1987.
- D. F. Young. Fluid mechanics of arterial stenosis. *Journal of Biomechanical Engineering*, 101:157–175, 1979.
- D. F. Young and F. Y. Tsai. Flow characteristics in models of arterial stenoses – 1 Steady flow. *Journal of Biomechanics*, 6:395–410, 1973.